Available online at www.sciencedirect.com
SCIENCE DIRECT®
Journal of Sound and Vibration 284 (2005) 467–486
JOURNAL OF SOUND AND VIBRATION
www.elsevier.com/locate/jsvi

Sound transmission through a flexible panel into an enclosure: structural–acoustics model

Moustafa Al-Bassyiouni, B. Balachandran*

Department of Mechanical Engineering, University of Maryland, College Park, MD 20742, USA

Received 30 September 2003; accepted 18 June 2004
Available online 21 November 2004

Abstract

In this article, a combined analytical and numerical effort is presented for modeling structural acoustics of sound transmission through a flexible panel into an enclosure. A spherical wave, which is generated by a noise source located in the near field, is transmitted into a rectangular enclosure through a flexible panel. Piezoelectric patches, which are bonded symmetrically to the top and bottom surfaces of the panel, are used as actuators. Microphone sensors are used inside and outside the enclosure for acoustic pressure measurements. The developed model accounts for panel interactions with both the external sound field and the enclosed sound field, and this feature makes it appealing for model-based active noise control schemes. For different actuator–sensor pairs, the numerically obtained frequency–response functions from the model are found to be in good agreement with the corresponding experimental observations.
© 2004 Elsevier Ltd. All rights reserved.

1. Introduction

Control of noise and vibration is important for many civil, industrial, and defense applications. In *Active Structural Acoustical Control* (ASAC) [1], which can be considered a modified version of *Active noise Control* (ANC), one takes advantage of vibrating structural elements as secondary noise sources to cancel the sound fields generated by a primary noise source (e.g., Refs. [2–5]). However, to develop model-based ASAC schemes, one needs a good understanding of the structural–acoustic interactions in the considered system.

*Corresponding author. Tel.: +1 301 405 5309; fax: +1 301 314 9477.
E-mail address: balab@eng.umd.edu (B. Balachandran).

0022-460X/$ - see front matter © 2004 Elsevier Ltd. All rights reserved.
doi:10.1016/j.jsv.2004.06.040

Considerable effort has been devoted to the modeling of structural acoustics, in particular, for enclosures with flexible boundaries. The efforts of Dowell and Voss [6] and Lyon [7] represent some of the early investigations into modeling of vibrations of plates backed by a cavity. Guy developed a model for the steady-state transmission of oblique sound waves through a thin panel backed by a rectangular room [8]. In his work, the oblique incident wave was considered as a combination of a normally incident wave and a wave with grazing incidence. Balachandran et al. [9] have developed a mechanics-based analytical model to address the interactions between a panel and the sound field inside a rectangular enclosure. In this work, piezoelectric patches bonded to the panel are used as actuators, which are also included in the modeling. Geng et al. [10] extended the work of Balachandran et al. [9] to the case of an irregular enclosure with two flexible panels. In the efforts of Ro and Baz [11], finite-element models are constructed for similar problems, while Nefske et al. [12] used a finite-element technique to model an automobile passenger compartment with flexible boundaries. Kim and Kim [13] developed a mass–damper–spring system to address the case of a thin panel that partially covers a "small" rectangular cavity. Due to the low number of degrees of freedom used in this model, its range of applicability is limited to the low-frequency range. Kim and Brennan used the impedance-mobility approach for modeling structural–acoustic coupling, and they applied that approach to a rectangular enclosure with a flexible panel (e.g., Refs. [14,15]). Their work has been extended by Lau and Tang to investigate the effect of the strength of the structural–acoustic coupling [16]. As in the work of Balachandran et al. [9], Chang and Nicholas [17] used Green's functions to study the frequency response of structural–acoustic systems. This approach is suitable for frequency–response analysis, but not convenient for control designs that require time–domain models.

All of the above-mentioned studies are restricted to the interaction between the structure and cavity and they do not consider the sound radiation from the panel into the external field; this aspect is important for feedforward control schemes. In addition, in all of the previous studies, the case where the panel–enclosure system is located in the near field of the noise source has not been considered; in these cases, the sound–pressure field acting on the panel is not uniform [18]. In systems such as a helicopter cabin, the noise source is "close" to the enclosure that the assumption of plane wave incidence may not be a good approximation. For the case of a spherical wave, the air particle velocity is no longer in phase with the acoustic pressure, and, in addition, the pressure distribution on the flexible panel is neither constant nor linear, as it is for a plane wave with normal or oblique incidence.

In this paper, the system of interest is a rectangular enclosure with rigid walls and one flexible panel. Noise is generated by an external noise source, which is located near the flexible panel, and transmitted into the enclosure through the flexible panel. Piezoceramic patches that are mounted on the flexible boundary are used as actuators. The noise source and/or the piezoceramic actuators can be used to excite the system. Polyvinylidene fluoride sensors are used on the flexible boundary, and microphone sensors are used inside and outside the enclosure. A mechanics-based model has been developed to analyze the sound fields inside the rectangular enclosure and the vibrations of the flexible boundary, as well as the structural–acoustic interactions. In addition, the sound field outside the enclosure is also taken into account to construct the system model. This work is an extension of the work carried out by Balachandran et al. [9], where structural–acoustic interactions were studied in the presence of a plane wave normal to the flexible panel. By contrast, in the current work, the more general case of a spherical wave is considered. In addition, the

sound radiated by the panel into the external field is also taken into account. Although the model has been developed for ASAC schemes, it is also applicable for the development of other control schemes.

The rest of this article is organized as follows. In the next section, the experimental arrangement is described, and then, the system model is developed in the following section. Next, numerical and experimental results are presented and discussed.

2. Experimental arrangement

In Figs. 1–3, the experimental arrangement and its different components are shown. As shown in Fig. 1, a loudspeaker is located above a rectangular enclosure and this loudspeaker is used as an external noise source. The rectangular enclosure has five rigid walls made from 2.54 cm thick acrylic sheets and a flexible panel made from 0.0625 cm thick aluminum material. This aluminum panel, which is clamped along all the four edges, has the following dimensions: $L_{xp} = 66.04$ cm and $L_{yp} = 50.80$ cm. The inner dimensions of the enclosure are 60.96 cm × 45.72 cm × 50.80 cm. The speaker, which has a diaphragm of 38.10 cm diameter, is mounted at a distance of 76.20 cm from the top of the enclosure and this speaker is driven by using one of the channels of a stereo amplifier.

In Fig. 2, the locations and the geometry of the piezoceramic (PZT-5H) patches are shown. These patches are symmetrically mounted on the top and bottom surfaces of the panel. The actuators are arranged in a grid with the row labels being {A, B, C} and the column labels being {1, 2, 3}, as shown in Fig. 2(a). Each of these actuators has the following dimensions: $L_{xpzt} = 5.08$ cm, $L_{ypzt} = 2.54$ cm, and thickness $h_{pzt} = 0.0254$ cm. In each pair, the actuators are wired out

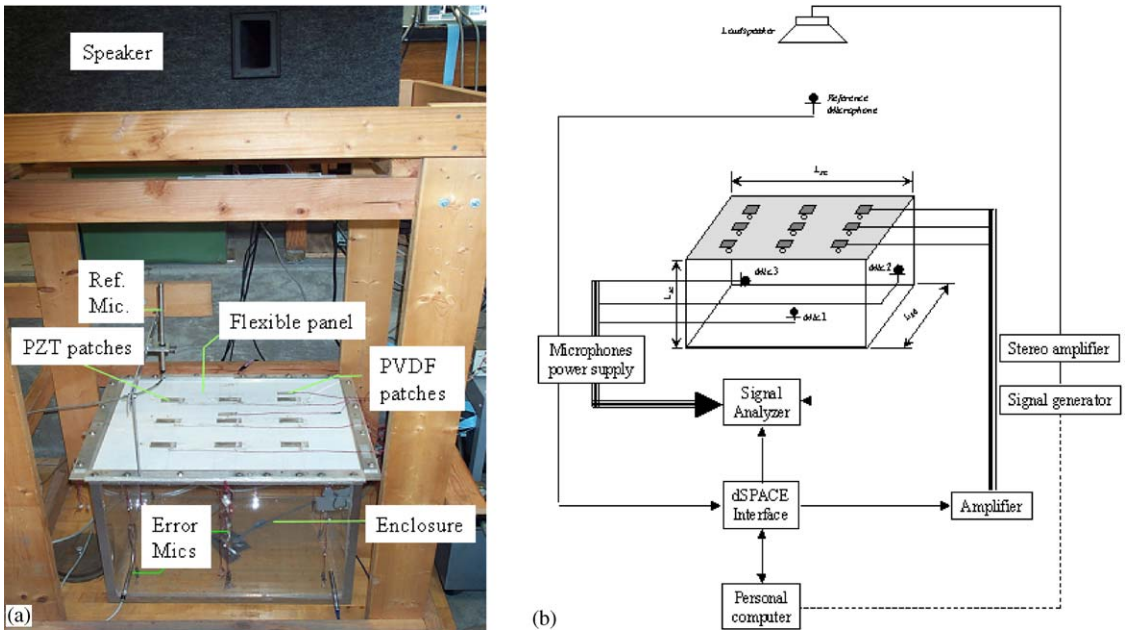

Fig. 1. Experimental arrangement: (a) photograph of the arrangement and (b) schematic representation.

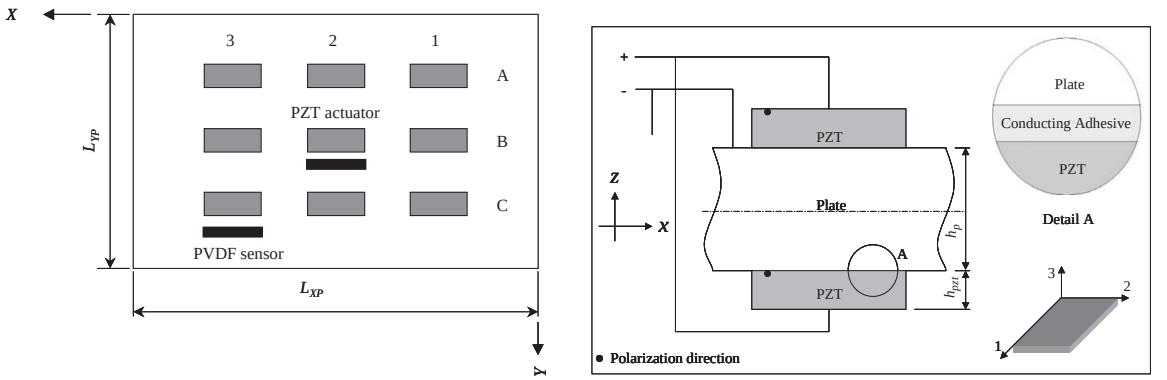

Fig. 2. Distributed actuators and sensors: (a) spatial locations on the flexible panel and (b) panel-PZT patch geometry.

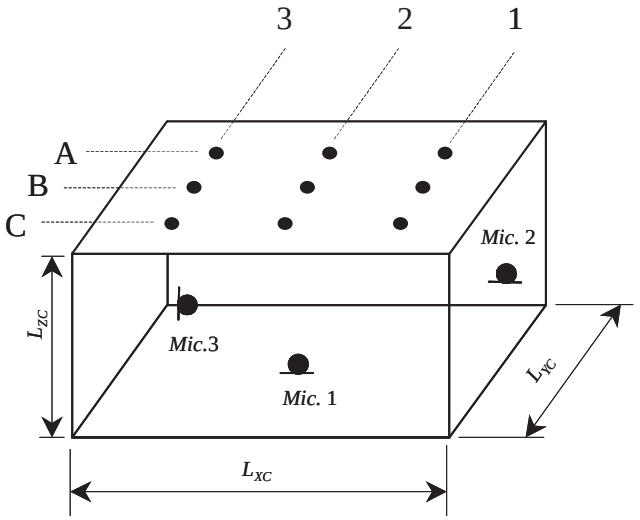

Fig. 3. Locations of microphones inside the enclosure.

of phase to cause extension in one patch and contraction in the other, resulting in a "localized" bending moment at the edges of the pair (see Fig. 2(b) for electrical input and actuator pair geometry). The dielectric constant of the piezoelectric material is $d_{31} = -274 \times 10^{-12}$ m/V and the material density is 7500 kg/m^3. Polymer-based piezo (PVDF) film sensors (DT2052 K/L) are bonded to the top surface of the panel close to the locations of the actuator pairs. The centers of the PVDF sensors, which are labeled P-B2 and P-C3, are located at (33.02 cm, 29.21 cm) and (49.52 cm, 41.28 cm), respectively.

Condenser microphones are used as sensors to measure the pressure levels inside and outside the enclosure. The external microphone (referred to here as the *reference microphone*), which provides the reference signal to the control system, is placed at a height of 50.80 cm from the

Table 1
Characteristics of different microphones used in the experimental setup

Microphone (Brüel & Kjær)		Ref. Mic.	Mic. 1	Mic. 2	Mic. 3
Model number		B&K 4134	B&K 4145	B&K 4145	B&K 4133
Location	inches	12, 9, 40	12, 9, $4\frac{1}{2}$	$1\frac{1}{4}$, 4, $9\frac{1}{4}$	$22\frac{3}{4}$, $1\frac{3}{4}$, $1\frac{1}{4}$
(x, y, z)	cm	30.5, 22.9, 101.6	30.5, 22.9, 10.8	3.2, 10.2, 23.5	57.8, 4.4, 3.2
Diameter	inches	$\frac{1}{2}$	1	1	$\frac{1}{2}$
	cm	1.3	2.5	2.5	1.3
Sensitivity (mV/Pa)		12.5	50	50	12.5
Polarization voltage (V)		200	200	200	200
Frequency range (Hz)		4–20k	2.6–18k	2.6–18k	4–40k
Dynamic range (dB)		21–160	11–146	11–146	22–160

panel-enclosure system. The internal microphones, which are labeled as Mic. 1, Mic. 2, and Mic. 3 and shown in Fig. 3, are arranged so that all of the enclosure modes can be sensed by one or the other. The locations and characteristics of the microphones are given in Table 1. The inputs to the actuators and the outputs from the sensors are realized by using a personal computer and an interface.

3. Analytical model

In this section, a model is developed for the panel–enclosure system shown in Fig. 1. PZT pair patches are considered to be bonded to the flexible panel, and each pair is assumed to produce a pure moment actuation when the patches are actuated as shown in Fig. 2. The flexible panel is exposed to an external pressure excitation created by a spherical wave generated by a sound source mounted above the enclosure. As shown in the schematic of the panel–enclosure system (Fig. 4), two coordinate systems are used to describe the system: the first one with the origin at 0_c is used for the enclosure, and the second one with the origin at 0_p is used for the panel. The panel may have larger dimensions than the enclosure.

Throughout the analysis, bold notation is used to denote vector quantities and uniform ambient values are indicated with the subscript notation $(\bullet)_0$. Assuming that the fluctuations in the pressure and density are small compared to their ambient values, and after including a damping term with the damping coefficient γ_a, the homogeneous wave equation describing the sound pressure inside the enclosure can be obtained as

$$\nabla^2 p - \frac{1}{c_0^2}\frac{\partial^2 p}{\partial t^2} - \gamma_a \frac{\partial p}{\partial t} = 0, \tag{1}$$

where $p(x, y, z, t)$ is the air pressure inside the cavity, the speed of sound is given by [19]

$$c = \sqrt{\left.\frac{\mathrm{d}p}{\mathrm{d}\rho}\right|_{p_0,\rho_0}} \tag{2}$$

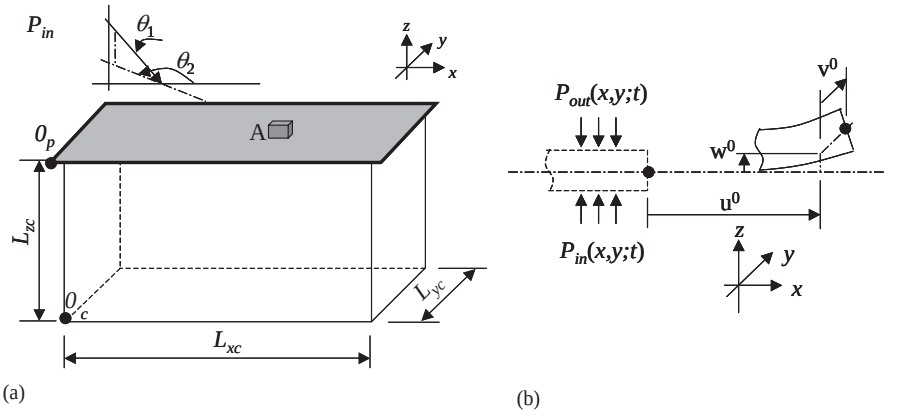

Fig. 4. (a) Schematic representation of panel–enclosure system used in model development, (b) detail A.

and $\rho_0(x, y, z, t)$ is the ambient air density. For the considered panel–enclosure system with one flexible boundary and five rigid boundaries, the boundary conditions take the form

$$\frac{\partial p}{\partial n} = \begin{cases} 0, & \text{at rigid boundary,} \\ -\rho_0(\partial^2 w/\partial t^2), & \text{at flexible boundary,} \end{cases} \tag{3}$$

where $w(x,y,t)$ is the normal displacement of the flexible boundary and n is the direction normal to the boundary. For the considered system, the pressure field inside the enclosure is assumed to have the form

$$p(x, y, z; t) = \sum_{i=1}^{\infty} \Phi_i(x, y, z) q_i(t) = \sum_{i=1}^{\infty} \psi_i(x)\phi_i(y)\Gamma_i(z) q_i(t), \tag{4}$$

where the spatial functions are orthogonal functions, which will be specified later.

In Eq. (4), the functions $\Phi_i(x, y, z)$ are used to describe the spatial field and the functions $q_i(t)$ are used to describe the associated temporal part of the pressure response. After substituting Eq. (4) into Eq. (1), integrating over the volume of the cavity, making use of the orthogonality conditions, and the boundary conditions given by Eq. (3), the equations governing the modal amplitudes can be obtained in the form

$$\frac{1}{c_0^2}\frac{\mathrm{d}^2 q_i}{\mathrm{d}t^2} + \gamma_a \frac{\mathrm{d}q_i}{\mathrm{d}t} + \left[k_i^2 - \left(\Gamma_i \frac{\mathrm{d}\Gamma_i}{\mathrm{d}z}\right)\Big|_{z=L_{zc}}\right] q_i = 0, \tag{5}$$

where

$$k_i^2 = \left[\int_{0_c}^{L_{xc}} \left(\frac{\mathrm{d}\psi_i}{\mathrm{d}x}\right)^2 \mathrm{d}x + \int_{0_c}^{L_{yc}} \left(\frac{\mathrm{d}\phi_i}{\mathrm{d}y}\right)^2 \mathrm{d}y + \int_{0_c}^{L_{zc}} \left(\frac{\mathrm{d}\Gamma_i}{\mathrm{d}z}\right)^2 \mathrm{d}z\right]. \tag{6}$$

The panel–piezo system is treated here as a multi-laminate system that consists of three plies in places where the piezo pair patches are bonded to the panel, and as a single ply panel otherwise. Making use of the assumptions used in earlier studies (e.g., Ref. [9]), the panel displacement can

be described by

$$D\nabla^4 w + \rho_p h_p \ddot{w} + \gamma_p \dot{w} = (p_{\text{in}} - p_{\text{out}}) - \sum_{i=1}^{K} \frac{(h_p + h_{pzt}) E_{pzt} d_{31}}{(1-v)} \nabla^2 \chi_i V_i(t), \tag{7}$$

where the panel stiffness constant D is given by

$$D = \frac{E_p h_p^3}{12(1-v^2)}. \tag{8}$$

Clamped boundary conditions are assumed along all edges of the panel. In Eq. (7), the quantity E is the panel material's Young's modulus, v is the Poisson's ratio, the quantities with subscripts pzt and p represent the constants related to the piezo patches and the flexible panel, respectively, and $V_i(t)$ is the voltage input to the ith piezo patch. The quantity $\chi_i = \chi(x_i, y_i)$ is unity, where the ith piezo patch pair is present, and it is zero elsewhere, and K is the total number of piezo patch pairs bonded to the panel. Along the lines of previous work [9], the Poisson's ratios for the panel and piezo material are assumed to be the same.

In Eq. (7), the external forcing term is the pressure loading $(p_{\text{in}} - p_{\text{out}})$, where $p_{\text{out}}(x, y; t)$ is the external pressure loading on the panel and $p_{\text{in}}(x, y; t)$ is the internal pressure loading on the panel (refer to Fig. 4). The external loading p_{out} is the sum of two pressure components, one corresponding to the incident wave with pressure p_i, and the other corresponding to the reflected wave with pressure p_r. By examining the structure–acoustic interface, it can be shown that $p_r = p_i + p_d$, where p_d is the radiation-damping term. Then, Eq. (7) can be rewritten in terms of p_i and p_{in} as

$$D\nabla^4 w + \rho_p h_p \ddot{w} + \gamma_p \dot{w} + p_d = p_{\text{in}} - 2p_i - \sum_{i=1}^{k} \frac{(h_p + h_{pzt}) E_{pzt} d_{31}}{(1-v)} \nabla^2 \chi_i V_i(t). \tag{9}$$

In Eq. (9), p_d is frequency dependant and it approaches $\rho_0 c_0 \dot{w}$ for a plane wave, thus the term $(\gamma_p \dot{w} + p_d)$ is considered throughout this section as an effective damping term. In practice, the associated damping coefficient is usually experimentally determined, and this is also carried out here as discussed later. In addition, to obtain Eq. (9), the wave transmitted through the flexible panel has been neglected in the analysis. This approximation is reasonable for *acoustic rigid boundaries*, when the wave is incident on a medium that has a high characteristic impedance compared to that of the incident medium. In the present case, the specific acoustic impedance of air is roughly 0.003% of the specific acoustic impedance of aluminum.

The panel response is assumed to be of the form

$$w(x, y; t) = \sum_{i=1}^{\infty} \alpha_i(x) \beta_i(y) \eta_i(t), \tag{10}$$

where the $\eta_i(t)$ are temporal functions and the appropriate expressions for the spatial functions $\alpha_i(x)$ and $\beta_i(y)$ are obtained from the work of Blevins [20]. Next, making use of the boundary condition given by Eq. (3) at the flexible boundary, the panel–enclosure system is integrated with

the panel–piezo system to obtain

$$\frac{1}{c_0^2}\,\ddot{q}_j(t) + \gamma_a \dot{q}_j(t) + k_j^2 q_j(t) + \rho_0 \Gamma_j|_{z=L_{zc}} \sum_{i=1}^{\infty} B_{ij}^{(c)}(x) B_{ij}^{(c)}(y) \ddot{\eta}_i(t) = 0. \tag{11}$$

The last term on the left-hand side of Eq. (11) represents the structural–acoustic coupling in the system and the spatial coefficients in the last term will be defined shortly.

At this stage, it is assumed that the spatial functions in Eq. (4) are given by rigid-body enclosure modes; that is,

$$\psi_i(x) = \frac{A_i}{\sqrt{L_{xc}}} \cos\left(\frac{l_i \pi x}{L_{xc}}\right), \quad \phi_i(y) = \frac{A_i}{\sqrt{L_{yc}}} \cos\left(\frac{m_i \pi y}{L_{yc}}\right), \quad \Gamma_i(z) = \frac{A_i}{\sqrt{L_{zc}}} \cos\left(\frac{n_i \pi z}{L_{zc}}\right), \tag{12}$$

where the indices l_i, m_i, and n_i are associated with the spatial functions of the ith rigid enclosure mode, along the x, y, and z directions, respectively. The constants A_i are chosen to satisfy the orthogonality conditions. Then, making use of Eqs. (6) and (12) in Eq. (11), it is found that

$$\frac{1}{c_0^2}\,\ddot{q}_j(t) + \gamma_a \dot{q}_j(t) + \left(\frac{l_j^2 \pi^2}{L_{xc}^2} + \frac{m_j^2 \pi^2}{L_{yc}^2} + \frac{n_j^2 \pi^2}{L_{zc}^2}\right) q_j(t) + \rho_0 \frac{(-1)^j A_j}{\sqrt{L_{zc}}} \sum_{i=1}^{\infty} B_{ij}^{(c)}(x) B_{ij}^{(c)}(y) \ddot{\eta}_i(t) = 0. \tag{13}$$

The equations governing the panel modal amplitudes are obtained by making use of Eqs. (4), (9), (10), and (12). After approximating $p_d \approx \rho_0 c_0 \dot{w}$ and making use of the orthogonality properties and the boundary conditions, the equation governing each panel modal amplitude is obtained as

$$\begin{aligned}
&\rho_p h_p \ddot{\eta}_j(t) + [\gamma_{pj} + \rho_0 c_0]\, \dot{\eta}_j(t) + D[I_j(x) + I_j(y)]\eta_j(t) + 2D \sum_{i=1}^{\infty} I_{ij}(x) I_{ij}(y) \eta_i(t) \\
&\quad = \sum_{i=1}^{\infty} \frac{(-1)^i A_i}{\sqrt{L_{zc}}} B_{ij}^{(p)}(x) B_{ij}^{(p)}(y) q_i(t) - 2\left[\int_{A_p} \alpha_j \beta_j p_i^s(x,y)\, \mathrm{d}A_p\right] p_i^t(t) \\
&\quad\quad - \sum_{i=1}^{k} \left[\int_{A_p} \alpha_j \beta_j \frac{(h_p + h_{pzt}) E_{pzt} d_{31}}{(1-\nu)}\, \nabla^2 \chi(x_i, y_i)\, \mathrm{d}A_p\right] V_i(t),
\end{aligned} \tag{14}$$

where the different spatial integrals in Eqs. (13) and (14) are given by

$$B_{ij}^{(p)}(x) = \int_{0_c}^{L_{xc}} \psi_i(x) \alpha_j(x)\, \mathrm{d}x = B_{ji}^{(c)}(x), \quad B_{ij}^{(p)}(y) = \int_{0_c}^{L_{yc}} \phi_i(y) \beta_j(y)\, \mathrm{d}y = B_{ji}^{(c)}(y),$$

$$I_j(x) = \int_0^{L_{xp}} \alpha_j(x) \frac{\mathrm{d}^4 \alpha_j(x)}{\mathrm{d}x^4}\, \mathrm{d}x, \quad I_j(y) = \int_0^{L_{yp}} \beta_j(y) \frac{\mathrm{d}^4 \beta_j(y)}{\mathrm{d}y^4}\, \mathrm{d}y,$$

$$I_{ij}(x) = \int_0^{L_{xp}} \frac{\mathrm{d}^2 \alpha_i(x)}{\mathrm{d}x^2} \alpha_j(x)\, \mathrm{d}x, \quad I_{ij}(y) = \int_0^{L_{yp}} \frac{\mathrm{d}^2 \beta_i(y)}{\mathrm{d}y^2} \beta_j(y)\, \mathrm{d}y \tag{15}$$

and the incident pressure loading has been expanded as

$$p_i(x, y; t) = p_i^s(x, y) p_i^t(t). \tag{16}$$

Eqs. (13) and (14) are then rearranged in matrix form:

$$\begin{bmatrix} \mathbf{M}_{pp} & \mathbf{0} \\ \mathbf{M}_{cp} & \mathbf{M}_{cc} \end{bmatrix} \begin{pmatrix} \ddot{\boldsymbol{\eta}} \\ \ddot{\mathbf{q}} \end{pmatrix} + \begin{bmatrix} \mathbf{D}_{pp} & \mathbf{0} \\ \mathbf{0} & \mathbf{D}_{cc} \end{bmatrix} \begin{pmatrix} \dot{\boldsymbol{\eta}} \\ \dot{\mathbf{q}} \end{pmatrix} + \begin{bmatrix} \mathbf{K}_{pp} & \mathbf{K}_{pc} \\ \mathbf{0} & \mathbf{K}_{cc} \end{bmatrix} \begin{pmatrix} \boldsymbol{\eta} \\ \mathbf{q} \end{pmatrix} = \begin{bmatrix} \mathbf{F}_p & \mathbf{F}_V \\ \mathbf{0} & \mathbf{0} \end{bmatrix} \begin{pmatrix} p_i^t \\ \mathbf{V} \end{pmatrix}, \tag{17}$$

where the off-diagonal terms in the **M** and **K** matrices describe the structural–acoustic coupling and the different quantities are given by

$$\mathbf{M}_{pp} = \mathrm{diag}[\rho_p h_p], \quad \mathbf{M}_{cc} = \mathrm{diag}\left[\frac{1}{c_0^2}\right],$$

$$\mathbf{M}_{cp} = [M_{cp}(i,j)] = \rho_0 \left[\frac{(-1)^i A_i}{\sqrt{L_{zc}}} B_{ji}^{(c)}(x) B_{ji}^{(c)}(y)\right],$$

$$\mathbf{D}_{pp} = \mathrm{diag}[\gamma_{pj} + \rho_0 c_0] = \mathrm{diag}[2\zeta_{pj}\omega_{pj}\rho_p h_p + \rho_0 c_0], \quad \mathbf{D}_{cc} = \mathrm{diag}[\gamma_{aj}] = \frac{1}{c_0^2}\mathrm{diag}[2\zeta_{cj}\omega_{cj}],$$

$$\mathbf{K}_{pp} = [k_{pp}(i,j)] = 2D[I_{ji}(x) I_{ji}(y)] + D\,\mathrm{diag}[I_i(x) + I_i(y)],$$

$$\mathbf{K}_{cc} = \mathrm{diag}\left[\frac{l_i^2\pi^2}{L_{xc}^2} + \frac{m_i^2\pi^2}{L_{yc}^2} + \frac{n_i^2\pi^2}{L_{zc}^2}\right],$$

$$\mathbf{K}_{pc} = [k_{pc}(i,j)] = \left[-\frac{(-1)^j A_j}{\sqrt{L_{zc}}} B_{ji}^{(p)}(x) B_{ji}^{(p)}(y)\right],$$

$$\mathbf{F}_p = \left(-2\int_{A_p} \alpha_i \beta_i p_i^s \,\mathrm{d}A_p\right),$$

$$\mathbf{F}_V = [F_V(i,j)] = \left[-\int_{A_p} \alpha_i \beta_i \frac{(h_p + h_{pzt}) E_{pzt} d_{31}}{(1-\nu)} \nabla^2 \chi(x_j, y_j)\,\mathrm{d}A_p\right]. \tag{18}$$

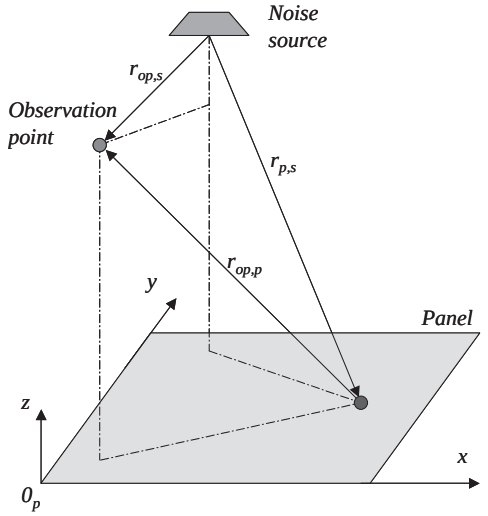

Fig. 5. Schematic representation of panel–external pressure field system used in model development.

Eq. (17) represents the time–domain model developed for the system shown in Fig. 4. After determining the modal amplitudes from these equations, the panel displacement $w(x,y;t)$ and the pressure inside the enclosure $p(x,y,z;t)$ can be obtained from the relations

$$\begin{pmatrix} w(x,y,z,t) \\ p(x,y,z,t) \end{pmatrix} = \begin{bmatrix} \mathbf{C}^{(w)} & \mathbf{0} \\ \mathbf{0} & \mathbf{C}^{(p)} \end{bmatrix} \begin{pmatrix} \boldsymbol{\eta} \\ \mathbf{q} \end{pmatrix}, \tag{19}$$

where

$$\mathbf{C}^{(w)} = [\alpha_i(x)\,\beta_i(y)], \quad \mathbf{C}^{(p)} = [\psi_i(x)\phi_i(y)\Gamma_i(z)]. \tag{20}$$

After examining the pressure forcing coefficients $\mathbf{F}_p$ given in Eq. (18), it is known that a plane wave incidence with a wave front parallel to the panel will not excite any vibration modes with even x and/or y indices. Furthermore, from the structure of the coupling mass matrix $\mathbf{M}_{cp}$ and stiffness matrix $\mathbf{K}_{pc}$ given in Eq. (18), it is known that the acoustic mode (0,0,1) is coupled only to the odd × odd panel vibration modes, the acoustic mode (1,0,0) is coupled only to the even × odd

Table 2
Undamped natural frequencies of the coupled system and the damping-factor values used in the analytical model for the different panel and cavity modes

Panel modes	Cavity modes	Natural frequencies (Hz)	Damping factors
(1,1)		41.6	0.0219
(2,1)		73.7	0.010
(1,2)		95.0	0.010
(2,2)		124.6	0.001
(3,1)		125.6	0.050
(3,2)		174.1	0.030
(1,3)		176.5	0.050
(4,1)		196.1	0.050
(2,3)		205.2	0.100
(4,2)		243.0	0.050
(3,3)		252.6	0.020
	(1,0,0)	281.3	0.010
(5,1)		284.7	0.040
(1,4)		285.5	0.001
(2,4)		313.8	0.001
(4,3)		319.5	0.001
(5,2)		330.7	0.001
	(0,0,1)	337.6	0.080
(3,4)		360.2	0.001
	(0,1,0)	375.1	0.006
(5,3)		405.6	0.005
(1,5)		421.6	0.008
(4,4)		425.5	0.001
	(1,0,1)	439.5	0.006
(2,5)		449.9	0.001
	(1,1,0)	468.9	0.001
(3,5)		495.8	0.004

panel vibration modes, and the acoustic mode (0,1,0) is coupled only to the odd × even panel vibration modes. This coupling can be understood on the basis of the spatial shapes of the different modes in the xyz coordinate system.

In further development, the pressure source outside the enclosure is assumed to generate a harmonic excitation. The panel–enclosure system response obtained for this excitation is used to construct frequency–response functions that are compared to experimental data. The response obtained is used to determine the pressure field outside the enclosure. A schematic for the panel–external pressure field system is shown in Fig. 5. In order to determine the temporal component $p_{op}(t)$ of this pressure field, an observation point located at a distance $r_{op,s}$ from the noise source is considered. This point is located in between the noise source and the enclosure. The acoustic pressure at the considered observation point is treated as a superposition of pressures generated by the following two sources: (1) the acoustic pressure $p_{op1}(t)$ generated by the external or primary (noise) source and (2) the acoustic pressure $p_{op2}(t)$ reflected back from the flexible panel as well as that generated by the panel vibrations excited by the noise source and/or by providing inputs into the PZT patches. The external noise source is considered as a circular "unbaffled simple" sound source, with radius r_s and uniform surface velocity $u(t)$; this source is located at an arbitrary location (x_s,y_s,z_s) above the panel and it is assumed to transmit sound downwards only. Then, the source strength can be written as $Q = \pi r_s^2 u(t)$. For a harmonic

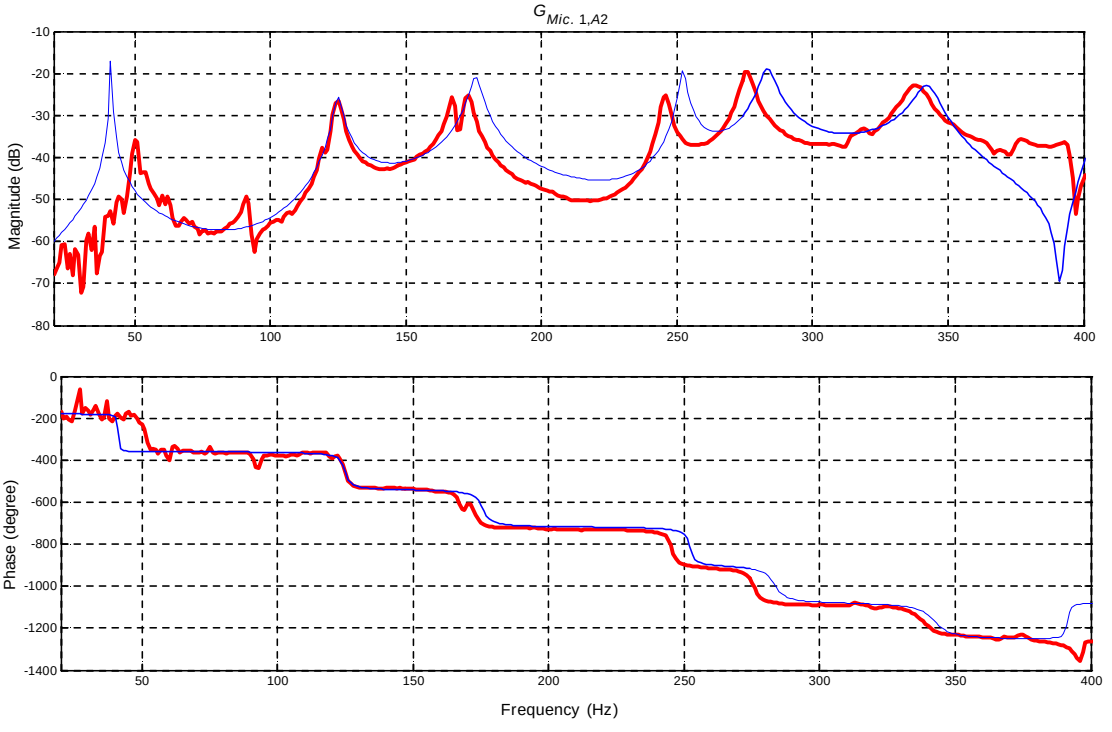

Fig. 6. Transfer function $G_{Mic.1,A2}$: comparison of model result with experimental data: dotted lines are experimental data and continuous lines are analytical predictions.

excitation; $u(t) = \bigcup e^{j\omega t}$, the equation describing $p_{op1}(t)$ is of the form [19]

$$p_{op1} = \frac{\rho_0 r_s^2}{4 r_{op,s}} e^{-jk r_{op,s}} a_s(t) = \frac{\rho_0 r_s^2}{4 r_{op,s}} e^{-j\omega T_{op1}} a_s(t), \tag{21}$$

where the surface acceleration $a_s(t)$ is $j\omega \cup e^{j\omega t}$, k is the wavenumber and equal to ω/c_0, and the time-delay constant T_{op1} is given by

$$T_{op1} = \frac{r_{op,s}}{c_0}. \tag{22}$$

The pressure $p_{op2}(t)$ generated from the panel motions can be determined by dividing the panel into infinitesimal elements of area dA, each of which is considered as a "baffled simple" source of strength $dQ = \dot{w}(x, y; t)\, dA$. This pressure component is given by

$$p_{op2}(t) = \frac{\rho_0}{2\pi} \int \int_{A_p} \ddot{w}(x, y, t) \frac{e^{-jk r_{op,p}}}{r_{op,p}} dA, \tag{23}$$

where $r_{op,p}(x,y)$ is the location of the observation point relative to point (x,y) on the panel. Making use of Eq. (10), $p_{op2}(t)$ can be represented in the form

$$p_{op2}(t) = \sum_{i=1}^{M} C_i^{(op)} \ddot{\eta}_i(t). \tag{24}$$

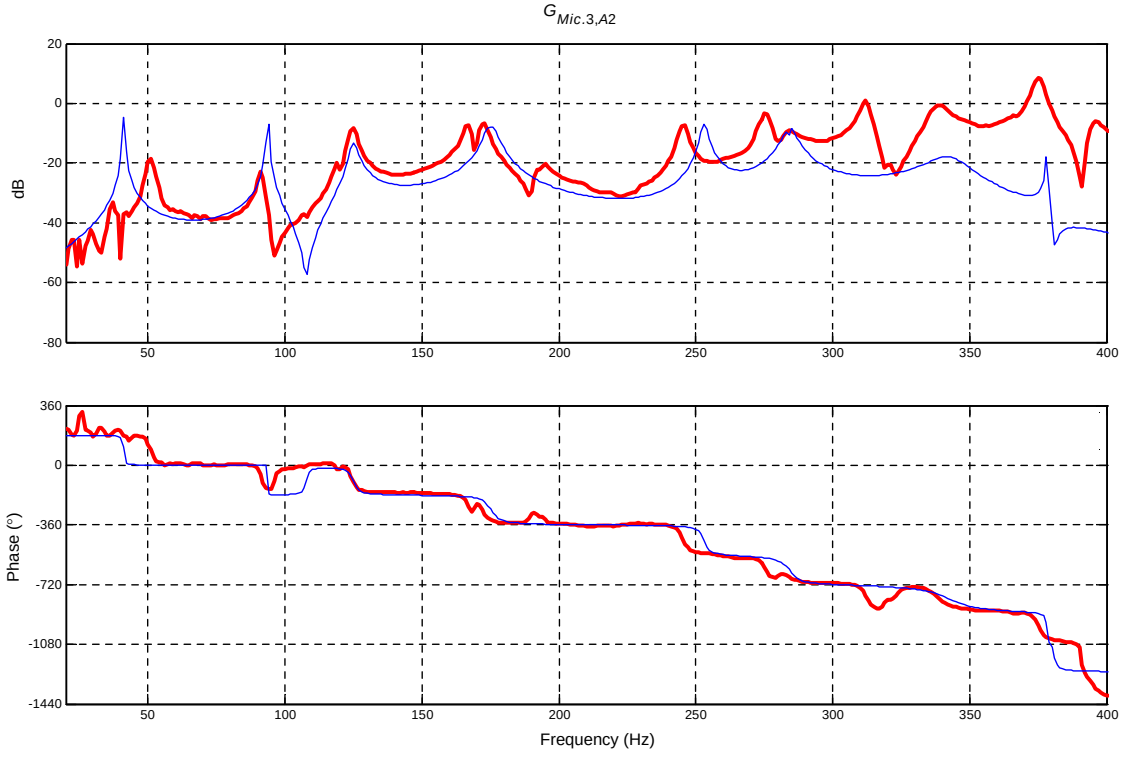

Fig. 7. Transfer function $G_{Mic.3,A2}$: comparison of model result (solid line) with experimental data (dotted line).

where

$$C_i^{(op)} = \frac{\rho_0}{2\pi} \int\int_{A_p} \alpha_i(x)\beta_i(y) \frac{e^{-jkr_{op,p}}}{r_{op,p}} \, dA. \tag{25}$$

Following a similar procedure, the pressure field $p_i(x,y,t)$ at a point (x,y) just above the panel surface can be determined as

$$p_i(x,y,t) = \frac{\rho_0 r_s^2}{4} \frac{e^{-jkr_{p,s}}}{r_{p,s}} a_s(t), \tag{26}$$

where $r_{p,s}(x,y)$ is the distance from the noise source to the point (x,y) on the panel.

Making use of Eq. (26) in Eqs. (17) and (18) leads to

$$\begin{bmatrix} \mathbf{M}_{pp} & \mathbf{0} \\ \mathbf{M}_{cp} & \mathbf{M}_{cc} \end{bmatrix} \begin{pmatrix} \ddot{\boldsymbol{\eta}} \\ \ddot{\mathbf{q}} \end{pmatrix} + \begin{bmatrix} \mathbf{D}_{pp} & \mathbf{0} \\ \mathbf{0} & \mathbf{D}_{cc} \end{bmatrix} \begin{pmatrix} \dot{\boldsymbol{\eta}} \\ \dot{\mathbf{q}} \end{pmatrix} + \begin{bmatrix} \mathbf{K}_{pp} & \mathbf{K}_{pc} \\ \mathbf{0} & \mathbf{K}_{cc} \end{bmatrix} \begin{pmatrix} \boldsymbol{\eta} \\ \mathbf{q} \end{pmatrix} = \begin{bmatrix} \mathbf{F}_a & \mathbf{F}_V \\ \mathbf{0} & \mathbf{0} \end{bmatrix} \begin{pmatrix} a_s \\ \mathbf{V} \end{pmatrix}, \tag{27}$$

where

$$\mathbf{F}_a = \left(-\frac{\rho_0 r_s^2}{2} \int\int_{A_p} \alpha_i(x)\beta_i(y) \frac{e^{-jkr_{p,s}}}{r_{p,s}} \, dA_p \right). \tag{28}$$

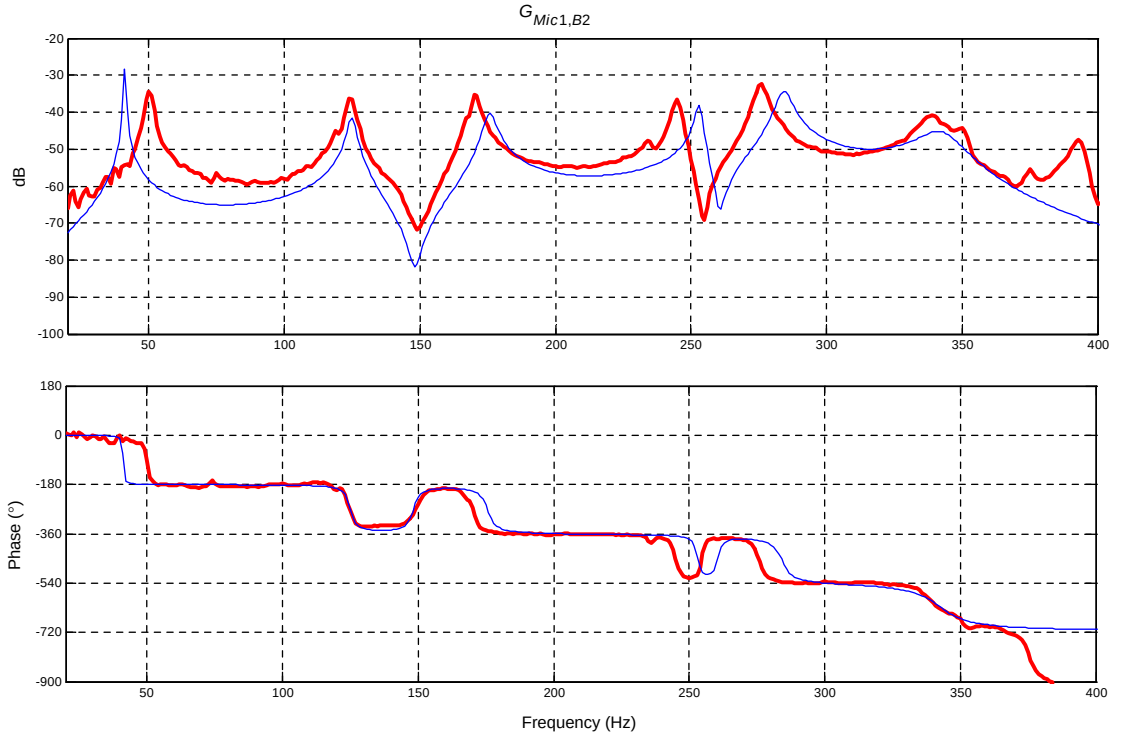

Fig. 8. Transfer function $G_{Mic.1,B2}$: comparison of model result (solid line) with experimental data (dotted line).

After solving Eq. (27) for the modal amplitudes in the frequency domain, the total pressure at an observation point above the enclosure can be determined from

$$p_{op}(t) = -\left[\bar{\mathbf{C}}^{(op)}\mathbf{K}_{pp} + \mathrm{j}\omega\,\bar{\mathbf{C}}^{(op)}\mathbf{D}_{pp}\right]\boldsymbol{\eta} - \left[\bar{\mathbf{C}}^{(op)}\mathbf{K}_{pc}\right]\mathbf{q} + \left[\bar{\mathbf{C}}^{(op)}\mathbf{F}_V\right]\mathbf{V} + \left(\bar{\mathbf{C}}^{(op)}\mathbf{F}_p + D^{(op)}\right)a_s, \quad (29)$$

where

$$\bar{\mathbf{C}}^{(op)} = \mathbf{C}^{(op)}\mathbf{M}_{pp}^{-1} = \left[\frac{C_i^{(op)}}{\rho_p h_p}\right], \quad D^{(op)} = \frac{\rho_0 r_s^2}{4r_{op,s}}\,\mathrm{e}^{-\mathrm{j}\omega T_{op1}}. \quad (30)$$

As can be seen, the quantity $\mathbf{F}_a$ given by Eq. (28) is a function of the frequency ω. It is expected that each of the modal weightings of $\mathbf{F}_a$ has a band-pass filter shape, where, in the considered bandwidth, the corresponding panel modes interact with the excitation-pressure field. To further understand the characteristics, the wave propagation term in Eqs. (25) and (28) is expanded as a Taylor series about a nominal value $r \approx R$ as

$$\frac{\mathrm{e}^{-\mathrm{j}kr}}{r} \approx \frac{\mathrm{e}^{-\mathrm{j}kR}}{R}\left\{\left[3 + 2\mathrm{j}kR - \tfrac{1}{2}(kR)^2\right] + \left(\frac{r}{R}\right)\left[-3 - 3\,\mathrm{j}kR + (kR)^2\right] + \left(\frac{r}{R}\right)^2\left[1 + \mathrm{j}kR - \tfrac{1}{2}(kR)^2\right]\right\} + O(r-R)^3. \quad (31)$$

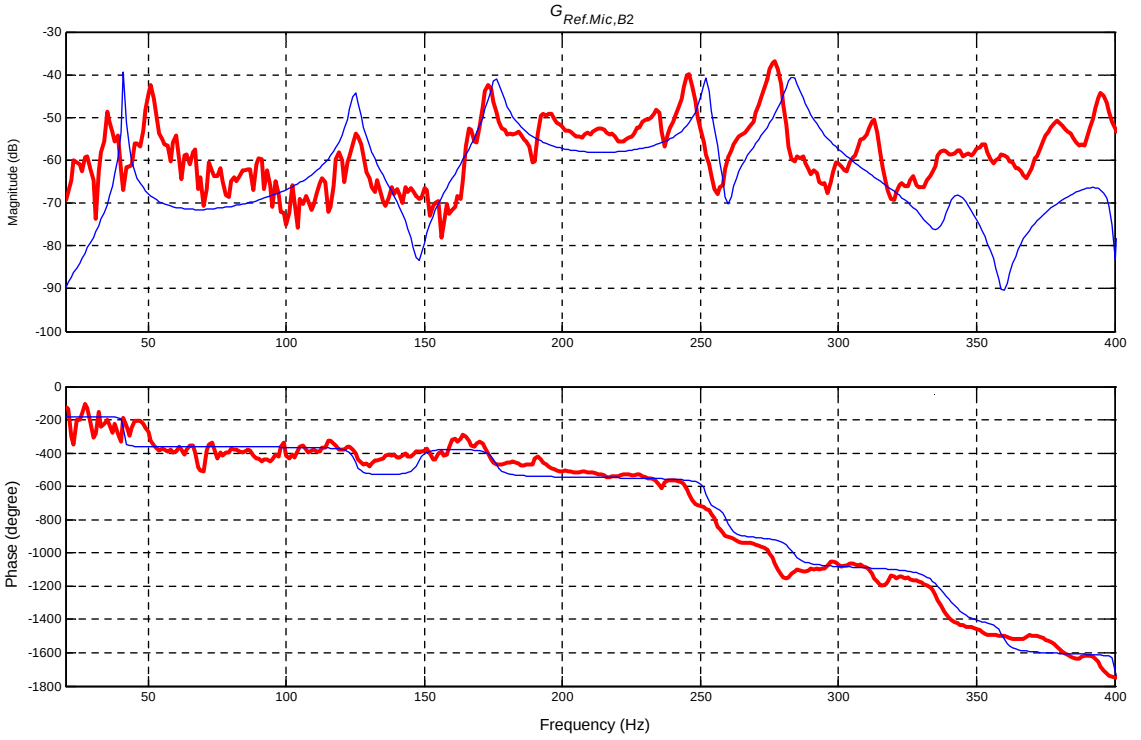

Fig. 9. Transfer function $G_{Ref.Mic.,B2}$: comparison of model result (solid line) with experimental data (dotted line).

From Eq. (31), it is clear that when the separation $|r - R|$ approaches zero, which is the acoustic far field condition, the series expansion reduces to $[e^{-jkR}/R]$ that can be obtained by considering a plane wave, instead of a spherical wave, with a separation R, which is necessarily not equal to the vertical distance between the sound source and the observation point.

As developed here, the current model has the capability of handling spherical incident waves. Other forms of incidence can also be captured by appropriately modeling the term $p_i^s(x, y)$ in Eq. (18); for example, an oblique incidence where the wavelength is less than the dimensions of the flexible panel can be studied. An important and unique aspect of the model is that the structure–acoustic interactions for the internal as well as external sound fields are taken into account.

4. Results and discussion

To obtain the numerical results of this section, the analytical model has been truncated to take into account the first 27 modes; these 27 modes include 22 panel modes and five enclosure modes. The resonance frequencies associated with these modes lie in a frequency span extending up to 500 Hz, with the highest resonance frequency being 495.75 Hz (please refer to Table 2). In the (x,y,z) coordinate system, the three indices of each acoustic mode correspond to the x, y, and z directions and the two indices of each vibration mode correspond to the x and y directions. In

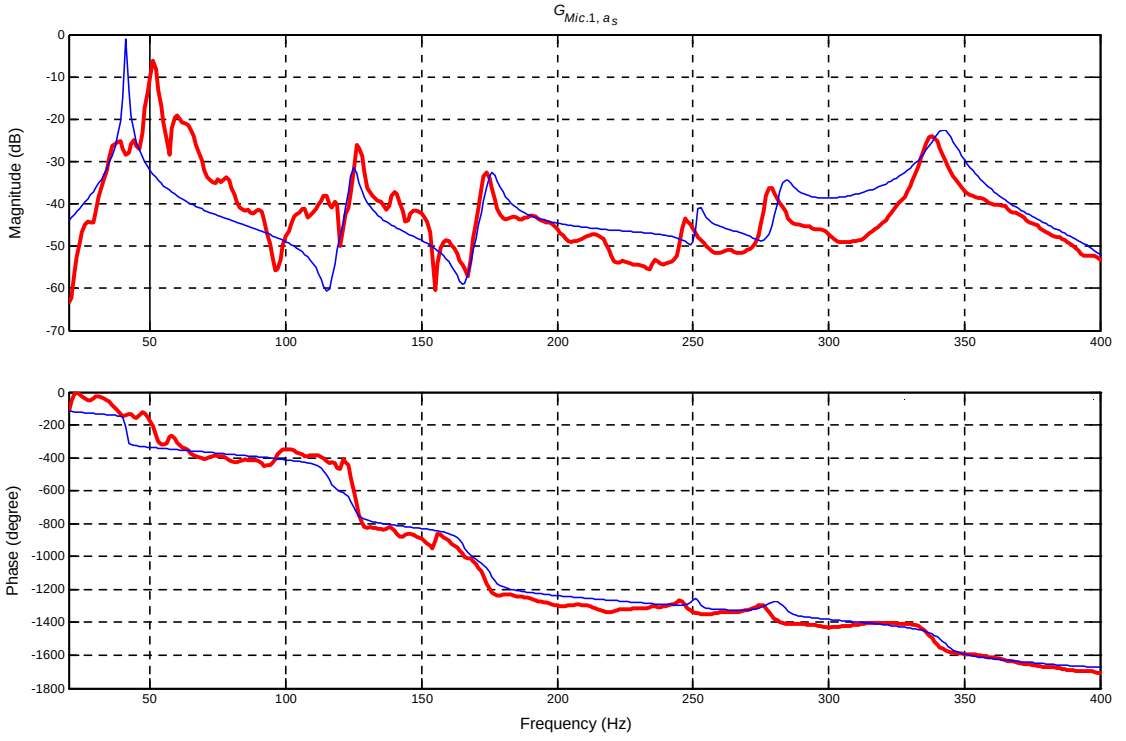

Fig. 10. Transfer function $G_{Mic.1,a_s}$: comparison of model result (solid line) with experimental data (dotted line).

Table 2, the numerical values of the different system natural frequencies, as predicted by the analytical model, are tabulated.

To examine why a spherical wave incidence should be considered, it is noted that the difference in pressure amplitude of the spherical wave incident at the panel varies over a 12% range across the panel area in the considered experimental arrangement. For excitation frequencies above 227 Hz, the phase difference between the waves incident at the panel center and corners is more than 45°, and for excitation frequencies above 455 Hz, this phase difference exceeds 90°. For this latter case, this would mean that while there is a pressure peak at the panel center, there is a pressure node at another panel corner. For these cases, the plane-wave approximation will not be a valid one.

In Figs. 6–12, the numerical results obtained from the analytical model are compared to the experimentally obtained frequency–response functions. In each case, the nomenclature $G_{y,x}$ is used to represent the transfer function between the output y and the input x. The inputs in these figures are either the acceleration of the speaker diaphragm, a_s, or the voltage input to one of the PZT patches, whose labels have been explained in Section 2. The outputs are the pressures at the reference microphone, microphone Mic. 1, and microphone Mic. 3. To obtain the experimental data, a white noise voltage signal was used as the excitation signal and the results obtained are shown over a 400 Hz bandwidth. Since the highest resonance frequency of the included modes is 495.75 Hz, the contribution of the unmodeled modes is insignificant in this frequency range. The

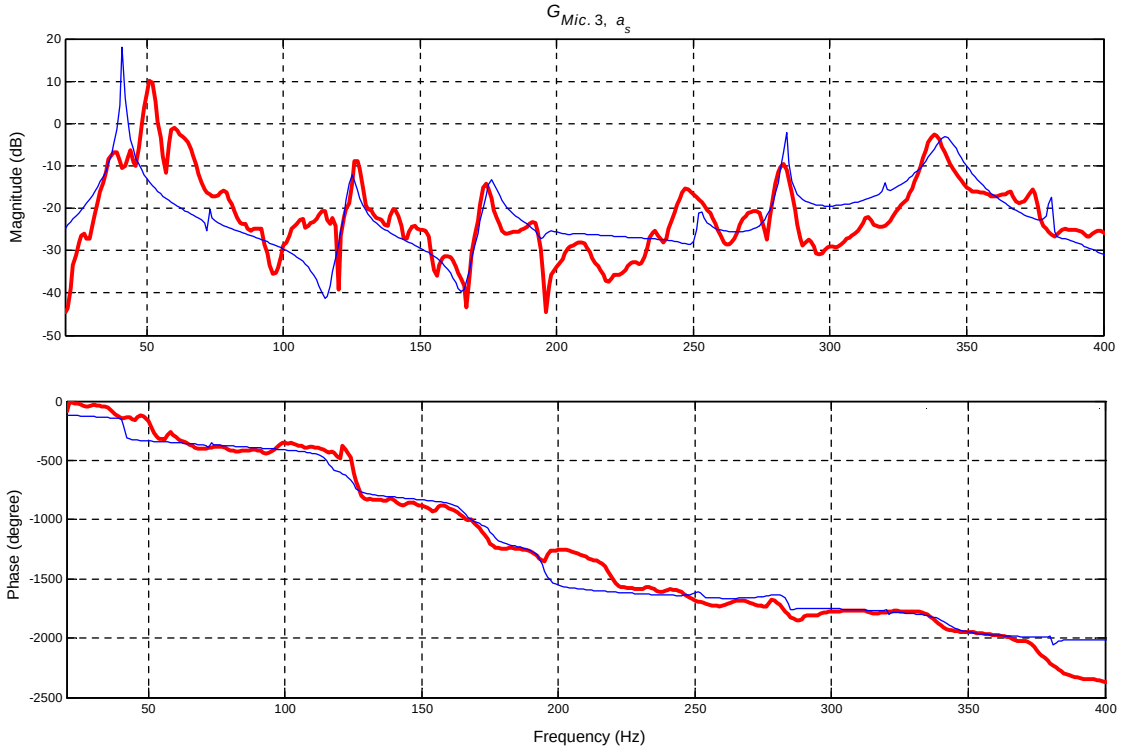

Fig. 11. Transfer function $G_{Mic.3,a_s}$: comparison of spherical-wave model result (solid line) with experimental data (dotted line).

frequency–response values for frequencies less than 20 Hz could not be realized due to the limitations of the equipment used in the experimental arrangement. The predictions shown in Figs. 6–8 illustrate the panel interactions with the enclosed sound fields, and the predictions shown in Fig. 9 illustrate the panel interaction with the external acoustics. The results shown in Figs. 10 and 11 illustrate the interactions between the three system components: the external sound fields, the panel, and the enclosed sound fields. Good agreement is seen between the experimental and numerical results. From the comparisons, it is clear that the present model does not perfectly capture the stiffness contribution at the first mode. It is believed that this difference may arise due to the assumption of weak structural–acoustic coupling considered in the mathematical model, which may not be valid in the low-frequency range. The differences at the other resonance frequency locations are less than 5%, which is expected because of the approximations used for clamped–clamped plates 20. For the different frequency–response functions considered, the model captures the phase information well. This indicates that the model developed here is suitable for model-based feedforward control schemes, where phase information is important.

To bring forth the importance of considering a spherical wave propagation, the pressure field results at the microphone locations Mic. 1, Mic. 2, and Mic. 3 are considered. For Mic. 3, in Figs. 11 and 12, the results obtained for spherical wave incidence and plane wave incidence are

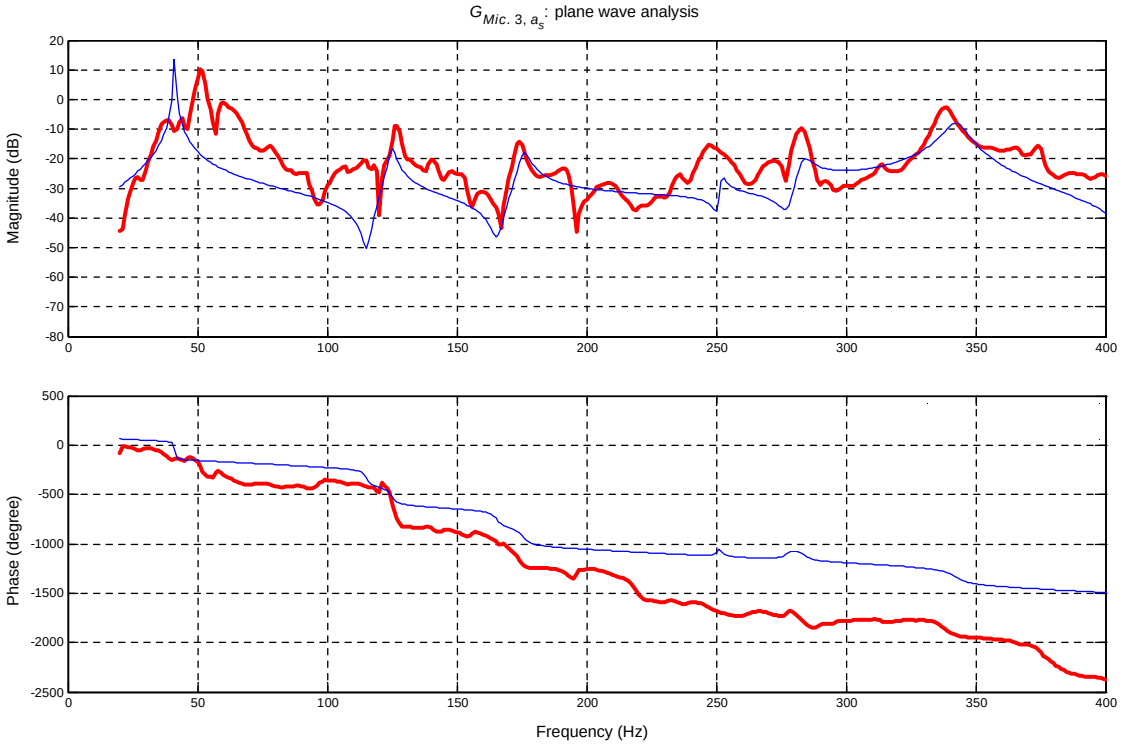

Fig. 12. Transfer function $G_{Mic.3,a_s}$: comparison of plane-wave model result (solid line) with experimental data (dotted line).

shown, respectively. In Fig. 11, the vibration modes with even indices (such as the (2,1) mode at 73.7 Hz and the (4,3) mode at 319.5 Hz) and the acoustic modes with nonzero x and y indices (such as the (1,0,0) mode at 281.3 Hz and the (0,1,0) mode at 375.1 Hz) are excited. As mentioned before, these modes cannot be excited by plane wave incidence, and this point can be inferred from Fig. 12. Comparisons with experimental results show that the phase changes are better predicted by the spherical wave propagation model. As seen in Fig. 10, the even-indexed vibration modes are not predicted at the location of the microphone Mic.1, due to its symmetric location with respect to the panel; however, the vibration mode (1,0,0) is predicted as a result of taking the spherical wave field into account. It is also pointed out that the time delays associated with the results shown in both Figs. 10 and 11 are different from those associated with a plane wave incidence, since the nominal values of R in Eq. (31) are different from the corresponding vertical separations among the sound source, the panel, and the observation point. For example, the time delay associated with Eq. (28) is 2.6 ms, corresponding to a separation of 89.91 cm, which is 2.28 cm larger than the vertical separation between the loudspeaker and the panel. This time delay difference cannot be predicted by using a plane wave approximation. In Fig. 13, the analytical prediction of the pressure field at the microphone location Mic. 2 is shown in the cases of a spherical wave field and a plane wave field. It is clear from the magnitude and phase results shown

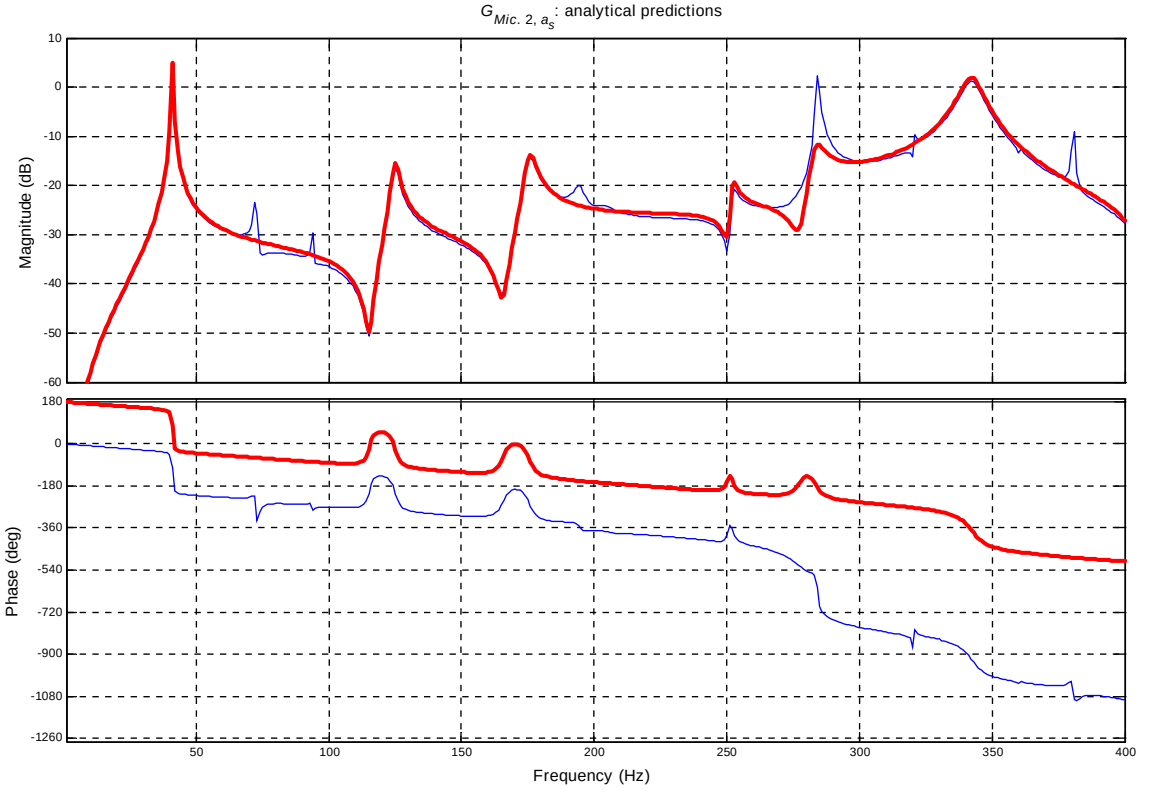

Fig. 13. Transfer function $G_{Mic.2,a_s}$: model results for spherical wave case (solid line) and plane wave case (dotted line).

in this figure that when a plane wave field model is used, the responses of many vibration and acoustic modes are not predicted.

In this effort, a structural–acoustics model has been developed for studying transmission of sound through a flexible panel into an enclosure. The model is used to describe the pressure fields inside and outside the three-dimensional rectangular enclosure, as well as the flexible panel vibrations. It has been shown how the model can address general cases such as spherical wave incidence and radiation into an infinite external acoustic space. In particular, the importance of considering a spherical wave incidence instead of a plane wave incidence is pointed out.

Acknowledgements

Partial support received for this work from the US Army Research Office (ARO) through Grant No. DAAH 049610334 is gratefully acknowledged. Drs. Tom Doligalski and Gary Anderson were the technical monitors for the ARO Grant.

References

[1] C.R. Fuller, A.H. von Flotow, Active control of sound and vibration, *IEEE Control Systems* 15 (6) (1995) 9–19.
[2] J. Pan, C. Hansen, D. Bies, Active control of noise transmission through a panel into a cavity: I. Analytical study, *Journal of the Acoustical Society of America* 87 (1990) 2098–2108.
[3] J. Pan, C. Hansen, Active control of noise transmission through a panel into a cavity: II Experimental study, *Journal of the Acoustical Society of America* 90 (1990) 1488–1492.
[4] S. Hirsch, J. Sun, Numerical studies of acoustic boundary control for interior sound suppression, *Journal of the Acoustical Society of America* 104 (1998) 2227–2235.
[5] M. Al-Bassyiouni, B. Balachandran, Zero spillover control of enclosed sound fields, *Proceedings of the SPIE's Eighth Annual International Symposium on Smart Structures and Materials*, Newport Beach, CA, vol. 4362, March 2001, Paper No. 4326-7.
[6] E. Dowell, H. Voss, The effect of a cavity on panel vibration, *AIAA Journal* 1 (1963) 476–477.
[7] R. Lyon, New reduction of rectangular enclosures with one flexible wall, *Journal of the Acoustical Society of America* 35 (1963) 1791–1797.
[8] R. Guy, The steady state transmission of sound at normal and oblique incidence through a thin panel backed by a rectangular room—a multi-modal analysis, *Acoustica* 43 (1979) 295–304.
[9] B. Balachandran, A. Sampath, J. Park, Active control of interior noise in a three-dimensional enclosure, *Smart Materials and Structures* 5 (1996) 89–97.
[10] H. Geng, Z. Roa, Z. Han, New modeling method and mechanism analyses for active control of interior noise in an irregular enclosure using piezoelectric actuators, *Journal of the Acoustical Society of America* 113 (2003) 1439–1454.
[11] J. Ro, A. Baz, Control of sound radiation from a plate into an acoustic cavity using active constrained layer damping, *Smart Materials and Structures* 8 (1999) 292–300.
[12] D. Nefske, J. Wolf, L. Howell, Structural–acoustic finite element analysis of the automobile passenger compartment: a review of current practice, *Journal of Sound and Vibration* 80 (1982) 247–266.
[13] S.-M. Kim, Y.-H. Kim, Structural–acoustic coupling in a partially opened plate-cavity system: experimental observation by using nearfield acoustic holography, *Journal of the Acoustical Society of America* 109 (2001) 65–74.
[14] S.M. Kim, M.J. Brennan, A compact matrix formulation using the impedance and mobility approach for the analysis of structural–acoustic systems, *Journal of Sound and Vibration* 223 (1999) 79–113.

[15] S.M. Kim, M.J. Brennan, Active control of harmonic sound transmission into an acoustic enclosure using both structural and acoustic actuators, *Journal of the Acoustical Society of America* 107 (2000) 2523–2534.
[16] S.K. Lau, S.K. Tang, Impacts of structural–acoustic coupling on the performance of energy density-based active sound transmission control, *Journal of Sound and Vibration* 266 (2003) 147–170.
[17] L. Chang, J. Nicholas, Radiation of sound into a cylindrical enclosure from a point-driven end plate with general boundary conditions, *Journal of the Acoustical Society of America* 91 (1992) 1504–1513.
[18] J. Park, Active Control of Noise in a Three-imensional Enclosure, M.S. Thesis, University of Maryland, 1995.
[19] L.E. Kinsler, A.R. Frey, A.B. Coppens, J.V. Sanders, *Fundamentals of Acoustics*, 4th ed., Wiley, New York, 2000.
[20] A.J. Blevins, *Formulas for Natural Frequency and Mode Shapes*, Krieger, Melbourne, FL, 1979.